Detection of fatigue microdamage in whole rat femora using contrast-enhanced micro-computed tomography ☆

Travis L. Turnbull, Joshua A. Gargac, Glen L. Niebur, Ryan K. Roeder *

Department of Aerospace and Mechanical Engineering, Bioengineering Graduate Program, University of Notre Dame, Notre Dame, IN 46556, USA

ARTICLE INFO

ABSTRACT

Microdamage in bone tissue is typically studied using destructive, two-dimensional histological techniques. Contrast-enhanced micro-computed tomography (micro-CT) was recently demonstrated to enable non-destructive, three-dimensional (3-D) detection of microdamage in machined cortical and trabecular bone specimens *in vitro*. However, the accumulation of microdamage in whole bones is influenced by variations in the magnitude and mode of loading due to the complex whole bone morphology. Therefore, the objective of this study was to detect the presence, spatial location, and accumulation of fatigue microdamage in whole rat femora *in vitro* using micro-CT with a $BaSO_4$ contrast agent. Microdamage was detected and observed to accumulate at specific spatial locations within the cortex of femora loaded in cyclic three-point bending to a 5% or 10% reduction in secant modulus. The ratio of the segmented $BaSO_4$ stain volume (SV) to the total volume (TV) of cortical bone was adopted as a measure of damage. The amount of microdamage measured by micro-CT (SV/TV) was significantly greater for both loaded groups compared to the control group ($p < 0.05$), but the difference between loaded groups was not statistically significant. At least one distinct region of microdamage, as indicated by the segmented SV, was observed in 85% of loaded specimens. A specimen-specific finite element model confirmed elevated tensile principal strains localized in regions of tissue corresponding to the accumulated microdamage. These regions were not always located where one might expect *a priori* based upon Euler–Bernoulli beam theory, demonstrating the utility of contrast-enhanced micro-CT for non-destructive, 3-D detection of fatigue microdamage in whole bones *in vitro*.

1. Introduction

Microdamage can accumulate in cortical bone tissue with aging and/or repetitive mechanical loading (Schaffler et al., 1995; Burr et al., 1997; Norman and Wang, 1997; O'Brien et al., 2003). The accumulation of microdamage in machined specimens *in vitro* has been shown to adversely affect mechanical properties, including the elastic modulus (Schaffler et al., 1989; Pattin et al., 1996) and fracture toughness (Norman et al., 1998). Therefore, microdamage has been associated with increased fracture susceptibility, including stress fractures in active individuals, fragility fractures in the elderly, and the effects of long-term antiresorptive treatments for osteoporosis (Burr et al., 1997; Chapurlat and Delmas, 2009). However, relatively few studies have investigated fatigue microdamage accumulation in whole bones, no matter whether loaded

in vitro (Forwood and Parker, 1989; Burr et al., 1998; Danova et al., 2003) or *in vivo* (Silva et al., 2006; Uthgenannt and Silva, 2007).

Microdamage in bone tissue is conventionally imaged and quantified using histological sections, which are inherently invasive, destructive, tedious and two-dimensional (Lee et al., 2003). A method for non-destructive, three-dimensional (3-D) imaging would enable spatial correlation of microdamage accumulation with variations in the mechanical loading (magnitude and stress state), bone mineral density, microarchitecture, and morphology of whole bones. Moreover, non-destructive, 3-D damage detection could also reduce the time and labor required by histological methods.

Contrast-enhanced micro-computed tomography (micro-CT) was recently demonstrated to enable non-destructive, 3-D detection of microdamage accumulation in cortical and trabecular bone specimens *in vitro* (Wang et al., 2007; Leng et al., 2008; Landrigan et al., 2011). Measurements of damage accumulation by contrast-enhanced micro-CT were strongly correlated with histological measurements using basic fuchsin, validating the new methods (Landrigan et al., 2011). However, previous studies using contrast-enhanced micro-CT only investigated geometric, machined specimens. Intra- and inter-specimen variation in whole bone morphology can lead to

non-uniform variation in the tissue strain distribution (e.g., Kotha et al., 2004), which would be expected to influence microdamage accumulation. Therefore, the objective of this study was to detect the presence, spatial location, and accumulation of fatigue microdamage in whole rat femora using micro-CT with a $BaSO_4$ contrast agent. Whole rat femora were loaded in cyclic three-point bending *in vitro* to predetermined levels of secant modulus degradation, stained with $BaSO_4$, and imaged by micro-CT.

2. Materials and methods

2.1. Specimen preparation

Thirty fresh-frozen hind limbs were obtained from mature male Wistar rats exhibiting no skeletal pathology. All protocol were approved by the Institutional Animal Care and Use Committee at the University of Notre Dame. Femora were excised from right and left hind limbs, cleaned of all soft tissue, and randomly divided into a non-loaded control group and two loaded groups ($n=10$/group). Two specimens were removed from the study due to experimental error in the measurement of the secant modulus degradation and $BaSO_4$ staining, but both were replaced by an additional hind limb. Specimens were stored at –20 °C in airtight containers containing an equal parts mixture of phosphate buffered saline (PBS) and ethanol during interim periods.

2.2. Fatigue loading

Whole rat femora were thawed and rehydrated at ambient temperature for 24 h prior to mechanical loading. Femora were loaded in cyclic three-point bending at 2 Hz under load control in a PBS bath at ambient temperature using an electromagnetic test instrument (Bose ElectroForce 3300, Bose Corp., Eden Prairie, MN), until achieving a 5% or 10% reduction in the secant modulus. The loading fixture employed cylindrical, 4 mm diameter, lower roller supports at a fixed span of 14.5 mm (Fig. 1). The upper load support had a major and minor diameter of 9 and 4 mm, respectively, with a concave surface ($R=2.5$ mm) designed to approximate the curvature of the cranial diaphyseal surface (Fig. 1). Specimens were preconditioned with a 27 N static compressive load for 5 min, followed by cyclic three-point bending with a sinusoidal waveform at 2 Hz between a minimum and maximum loads of 18 and 36 N, respectively. The secant modulus measured from the final hysteresis loop during cyclic preconditioning was used to calculate the maximum fatigue load normalized to an initial maximum strain of 8000 ± 825 microstrain. Initial flexural strains were approximated as $\varepsilon = 6d\delta/L^2$ (Turner and Burr, 1993; Moreno et al., 2006), where d is the specimen diameter, δ is the vertical deflection at the midspan, and L is the support span. The secant modulus degradation during fatigue loading was calculated as the percent reduction in instantaneous secant modulus at a given number of loading cycles relative to the initial secant modulus. The initial secant modulus was defined as the maximum secant modulus measured in the first 1000 cycles. The total number of loading cycles was recorded upon reaching the predetermined secant modulus degradation for each specimen.

2.3. Contrast-enhanced micro-CT

Femora from both the non-loaded control and loaded groups were stained by $BaSO_4$ precipitation (Landrigan et al., 2011). Specimens were soaked in a solution

of equal parts acetone, PBS, and 0.5 M $BaCl_2$ (certified ACS crystal, Fisher Scientific, Fair Lawn, NJ) in DI water for 3 d, followed by a solution of equal parts acetone, PBS, and 0.5 M Na_2SO_4 (anhydrous powder, Fisher Scientific, Fair Lawn, NJ) in DI water for 3 d, both under vacuum ($\sim$50 mm Hg). Specimens were rinsed with DI water after each step to minimize particles or ions on specimen surfaces. The staining mechanism was a precipitation reaction, where $BaCl_2(aq)+Na_2SO_4(aq) \rightarrow BaSO_4(s)+2NaCl(aq)$. Barium and sulfate ions diffused and concentrated in void space – e.g., microcracks, damaged tissue, and vasculature – which provided an abundance of heterogeneous nucleation sites for precipitation on tissue surfaces (Leng et al., 2008).

An 8.5 mm segment of the femoral diaphysis, centered about the midspan from three-point bending, was imaged using micro-CT (μCT-80, Scanco Medical AG, Brüttisellen, Switzerland) at 10 μm resolution, 70 kVp voltage, 114 μA current, and 400 ms integration time with slices oriented transverse to the diaphysis. Selected specimens were also imaged by micro-CT after fatigue loading but prior to staining to verify that microdamage was not able to be detected in the absence of the contrast agent. All micro-CT analyses were performed on the entire volume of the 8.5 mm segment scanned for each femur using manufacturer's software (IPL v6.0, Scanco Medical). Grayscale images were smoothed by a Gaussian filter with sigma=1.5 and support=3. The total volume (TV) of cortical bone, inclusive of tissue porosity and exclusive of medullary volume, was measured after contouring the endosteal and periosteal surfaces (Fig. 2). The ratio of the $BaSO_4$ stain volume (SV) to TV (SV/TV) was adopted as a measure of damage. High intensity voxels representative of SV were segmented at a constant global threshold of 730, corresponding to a mean linear attenuation coefficient of 5.84 cm^{-1} or $\sim$3340 mg hydroxyapatite per cubic centimeter (mg HA/cm^3) (Deuerling et al., 2010). This threshold was well above the tissue mineral density of rat cortical bone, which was measured in this study to be $\sim$1180 mg HA/cm^3 using micro-CT.

2.4. Scanning electron microscopy

Specimens exhibiting the median SV/TV for each group were also imaged using scanning electron microscopy (SEM). Specimens were dehydrated in a graded series of alcohol solutions, embedded in poly(methyl methacrylate), sectioned sagittally with a diamond wire saw, polished with a series of diamond compounds to a 9 μm finish, washed with ethanol, and coated with iridium by sputter deposition. Specimens were imaged by SEM using backscattered electron imaging (BEI) at an accelerating voltage of 20 kV and a working distance of $\sim$6 mm (Evo 50, LEO Electron Microscopy Ltd., Cambridge, UK). Note that image contrast from backscattered electrons is primarily due to compositional differences in atomic number, with an increasing atomic number resulting in increased intensity. The elemental composition of the stain was verified by electron probe microanalysis (EPMA) using energy dispersive spectroscopy (EDS) (INCA x-sight model 7636, Oxford Instruments America, Concord, MA).

2.5. Finite element model

Finite element models of specimens exhibiting the median SV/TV were used to examine strain distributions within transverse cross-sections of the femur. Micro-CT images were downsampled to 80 μm resolution by cubic interpolation and converted to tetrahedral meshes based on a constant threshold of 7000 (Visualization Tool Kit, Kitware, Clifton Park, NY). Following Laplacian smoothing, the mesh was translated to a general-purpose finite element code (ADINA 8.6, Watertown, MA). Loads and boundary conditions were applied to simulate static three-point bending. In order to avoid stress concentrations at contact points, a uniformly distributed force was applied over a 4 mm length of the cranial diaphyseal surface at the location of the upper load support. Uniform, isotropic elastic properties were assigned, with Young's modulus of 6.3 GPa, and Poisson's ratio of 0.3. The resulting displacement was approximately equal to the experimentally measured value in both cases. A second model using 60 μm resolution images was created for one sample to ensure sufficient mesh refinement.

2.6. Statistical methods

All experimental groups exhibited non-normal distributions for SV/TV and the total number of loading cycles. Therefore, SV/TV and the number of loading cycles were separately compared between groups using Kruskal–Wallis non-parametric, one-way analysis of variance (ANOVA). *Post hoc* comparisons were performed using Mann–Whitney U-tests with a Bonferroni correction for multiple comparisons (JMP 8.0.2, SAS Institute Inc., Cary, NC). SV/TV was correlated with the number of loading cycles using linear least squares regression. The level of significance for all tests was $p < 0.05$.

3. Results

Microdamage was detected and observed to vary spatially in all femora loaded in cyclic three-point bending using contrast-enhanced
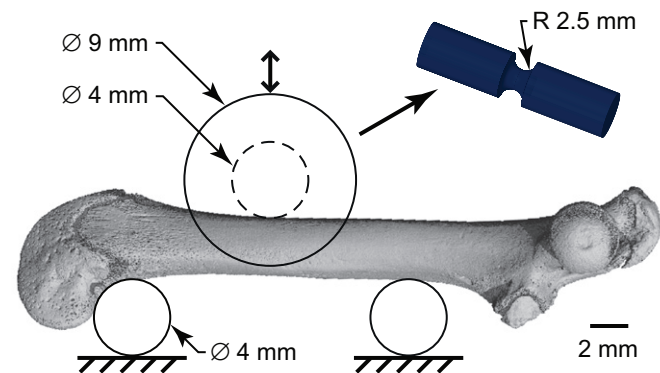

Fig. 1. Schematic diagram showing a segmented micro-CT reconstruction of a whole rat femur loaded in cyclic three-point bending with cylindrical lower load supports on the relatively flat caudal surface and a concave upper load support on the cranial surface of the diaphysis.
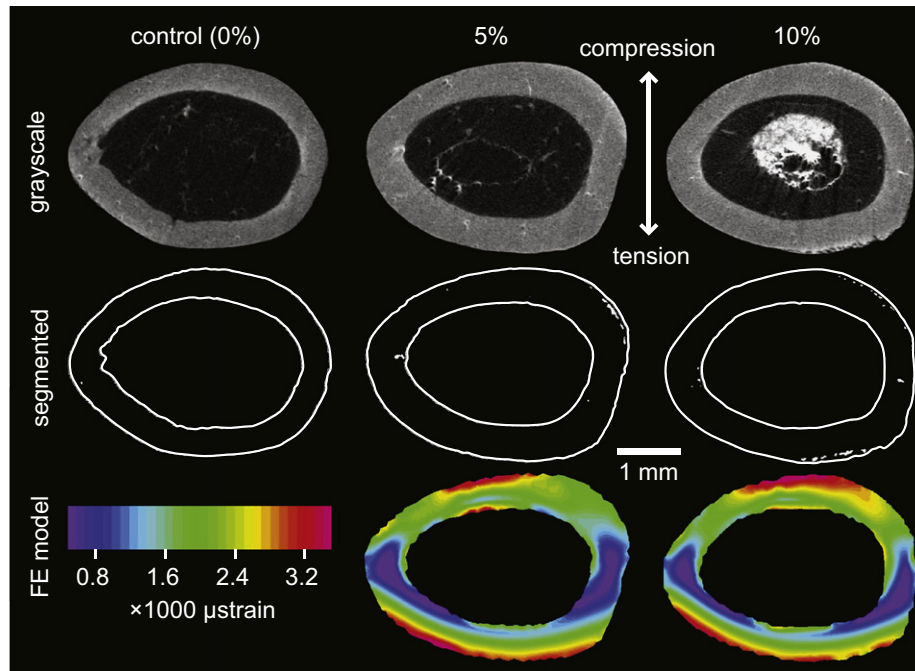
Fig. 2. Grayscale and corresponding segmented micro-CT images for transverse cross-sections of a non-loaded control specimen and femora loaded in cyclic three-point bending to a 5% and 10% reduction in secant modulus, showing regions labeled by $BaSO_4$ (bright voxels). Note that the images shown correspond to the midspan of the median specimen (SV/TV) in each group. Specimen-specific finite element model predictions of the first principal strain are shown for static three-point bending to the maximum applied load.

micro-CT. Microdamage was labeled by concentrated regions of $BaSO_4$ stain, which appeared as bright voxels in grayscale micro-CT images, and was quantified in segmented images (Fig. 2). Spatial variation in the accumulation of microdamage was observed in segmented, 3-D micro-CT reconstructions (Fig. 3). At least one distinct region of microdamage, as indicated by the segmented SV, was visible in 85% of loaded specimens, whereas control specimens exhibited a lower segmented SV (Fig. 3). Locations of segmented microdamage were consistently observed near cranial and caudal periosteal surfaces at the midspan, as expected, but also included unanticipated observations near medial and lateral endosteal surfaces at the mid-coronal plane, especially moving away from the midspan (Figs. 2 and 3). A specimen-specific finite element model predicted elevated tensile principal strains localized in regions of tissue corresponding to locations of segmented microdamage (Fig. 2).

Bright voxels detected by micro-CT were confirmed by back-scattered electron imaging to be microcracks and/or diffuse damage labeled with $BaSO_4$ (Fig. 4). EDS confirmed elevated levels of barium in labeled, damaged tissue relative to undamaged tissue. Histological observation of multiple sagittal sections from the median specimen (SV/TV) in both loaded groups revealed that microcracks located near the tensile (caudal) cortex were pre-dominantly transversely oriented, while microcracks located near the compressive (cranial) cortex were predominantly oriented longitudinally (Fig. 4).

The amount of microdamage measured by SV/TV increased from the non-loaded control group to the loaded groups ($p < 0.05$, Kruskal–Wallis). The mean ratio of $BaSO_4$ stain volume to the total bone volume (SV/TV) was significantly greater for either loaded group compared to the control group ($p < 0.05$, Mann–Whitney U-test), but the difference between loaded groups was not statistically significant (Fig. 5). The mean ($\pm$ standard deviation) total number of loading cycles for groups loaded to a 5% and 10% reduction in secant modulus was 122,000 (74,000) and 81,000 (55,000), respectively, and the difference was not statistically significant ($p = 0.52$, Mann–Whitney U-test). SV/TV exhibited a

weak positive correlation with the number of loading cycles for loaded specimens ($p = 0.08$, $R^2 = 0.16$).

4. Discussion

Microdamage resulting from cyclic three-point bending of rat femora *in vitro* was detected and observed to accumulate at specific spatial locations within the cortex using contrast-enhanced micro-CT with a precipitated $BaSO_4$ stain. Previous studies employed similar staining and imaging techniques to investigate microdamage within machined cortical and trabecular bone specimens (Wang et al., 2007; Leng et al., 2008; Landrigan et al., 2011). This study demonstrated the ability to detect microdamage in whole rat femora by adopting previously established methods. As such, this study constitutes the first non-destructive and 3-D assessment of microdamage in whole bones using contrast-enhanced micro-CT.

Whole bones pose greater challenges and opportunities for non-destructive detection of microdamage compared to geo-metric, machined specimens. For example, the bone morphology can lead to non-uniform variation in the tissue strain distribution (Fig. 2). Therefore, whole bone morphology can influence tissue mechanical behavior in ways not anticipated by Euler–Bernoulli beam theory, e.g., which assumes a uniform cross-section and homogeneous tissue properties (Van Lenthe et al., 2008). Loca-tions of segmented microdamage and elevated tensile principal strains were observed near cranial and caudal periosteal surfaces at the midspan, as expected (Figs. 2 and 3). However, locations of segmented microdamage also consistently included unantici-pated observations near medial and lateral endosteal surfaces at the mid-coronal plane in 85% of loaded femora (Figs. 2 and 3). Interestingly, the finite element model also predicted elevated tensile principal strains in these locations with increasing promi-nence moving away from the upper load support (midspan). A detailed investigation into the spatial correlation between
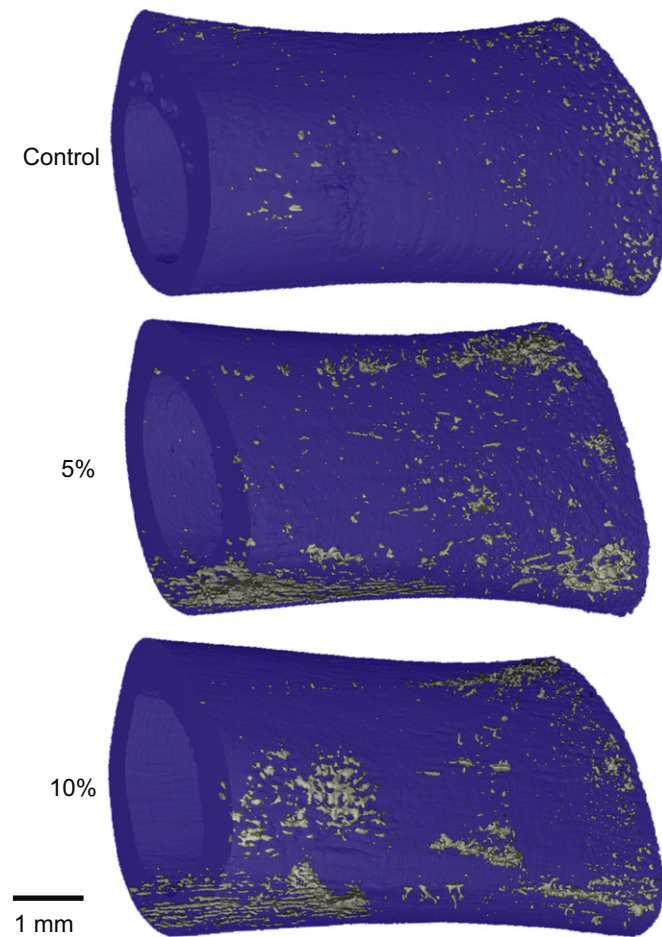
Fig. 3. Segmented, 3-D micro-CT reconstructions of a non-loaded control specimen and specimens loaded to 5% and 10% degradation in secant modulus showing distinct regions of microdamage labeled by $BaSO_4$. Specimens are oriented to show the caudal surface under tension between the lower supports with lateral and medial surfaces above and below, respectively. Note that the specimens shown are the median specimen (SV/TV) from their respective experimental group.

Fig. 4. Backscattered scanning electron micrographs of sagittal sections of femora showing (a) a longitudinal (coronal) microcrack located near the compressive (cranial) periosteal surface and (b) a transverse microcrack (arrow) located on the tensile (caudal) periosteal surface. Note that the images correspond to the median (SV/TV) specimen loaded to a (a) 5% and (b) 10% reduction in secant modulus. The labeling of microcracks by $BaSO_4$ is evident by the brightness associated with atomic number contrast in backscattered electron imaging. Double arrows indicate the direction of normal bending stresses.

segmented microdamage and finite element model predictions is ongoing.

The bright voxels observed in micro-CT images were verified by backscattered electron imaging and EDS to be due to the presence of $BaSO_4$ stain (Fig. 4), similar to previous studies (Wang et al., 2007; Leng et al., 2008; Landrigan et al., 2011). Note that backscattered electron imaging is destructive and was performed only to verify staining and image individual microcracks. Specimens were sectioned after non-destructive characterization using micro-CT. Individual microcracks located near the tensile (caudal) cortex were predominantly transversely oriented, while microcracks located near the compressive (cranial) cortex were predominantly oriented longitudinally (Fig. 4). These crack orientations, combined with the direction of tensile principal strains predicted by the finite element model, suggest mode I crack opening in either region of the cortex. Microcracks were also observed in backscattered electron imaging to be 100–500 μm in length and approximately 1 μm thick, similar to previous studies (Frost, 1960; Schaffler et al., 1994; O'Brien et al., 2000; Mohsin et al., 2006). A limitation of contrast-enhanced micro-CT using current, commercially available instruments with a resolution of 10 μm is that individual microcracks are not typically able to be resolved, though larger fatigue cracks have been resolved when the stain penetrated tissue adjacent to the crack by at least one voxel length (Landrigan et al., 2010, 2011).
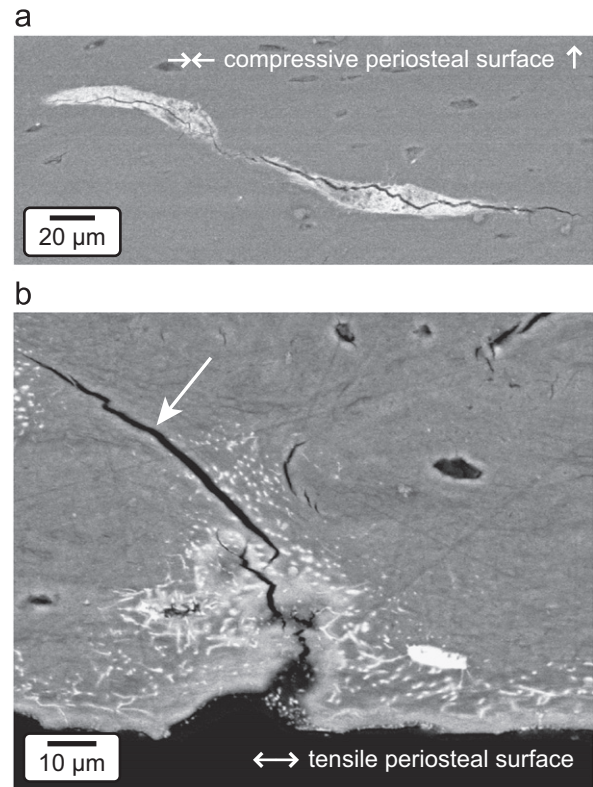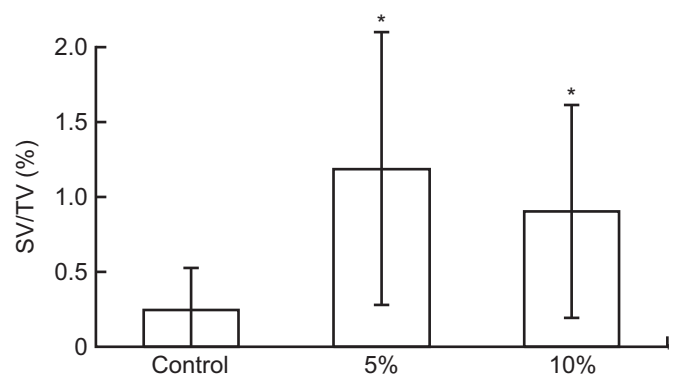

Fig. 5. The ratio of $BaSO_4$ stain volume to total volume (SV/TV) measured in segmented micro-CT images was increased for loaded groups compared to the non-loaded control group. Error bars show one standard deviation. $^{*}p < 0.05$, Mann–Whitney U-test versus control.

Variability in SV/TV (Fig. 5) was attributed to a combination of non-specific staining of free surfaces and porosity, especially near endosteal surfaces, and variability in whole bone morphology. The threshold utilized to segment SV was selected to minimize variability in SV/TV, as measured by the coefficient of variation across all experimental groups. Lower threshold values increased differences between the group means but also increased variability for SV/TV (cf., Fig. 5). Interestingly, there was relatively little

non-specific staining observed on periosteal surfaces in this study, most likely due to the periosteum. This observation contrasted previous studies where machined specimens were prone to non-specific staining on exterior surfaces (Leng et al., 2008; Landrigan et al., 2011). Finite element model predictions confirmed non-uniform spatial variation of strains within cross-sections (Fig. 2) and along the length of the diaphysis. As described above, the strain distribution varied between specimens and maxima were not always located where one might expect *a priori* based upon Euler–Bernoulli beam theory. This suggests that intra- and inter-specimen variabilities in whole bone morphology may have contributed significantly to variability in microdamage accumulation.

The lack of an increase in SV/TV between specimens loaded to a 5% and 10% degradation in secant modulus has more than one possible interpretation. The staining methods were adopted from previous studies on machined specimens (Wang et al., 2007; Leng et al., 2008; Landrigan et al., 2011) and were verified in a pilot study investigating stain penetration into whole rat femora using multiple levels of concentration and time. Nonetheless, as the technique has begun to be applied in multiple studies, we are learning that the optimal stain concentration and time appears to vary with the specimen size and tissue type, and may require further refinement. In particular, SEM observations suggested some specimens from this study may have been over-stained relative to specimens from our previous studies. On the other hand, the apparent microcrack density may not have increased with continued reduction in the secant modulus. Histological measurements of microcrack density within cyclically loaded rat ulnae (Danova et al., 2003) and canine femora (Burr et al., 1998) were similarly able to differentiate between control and loaded specimens, but unable to differentiate between specimens loaded to increasing levels of stiffness degradation. Moreover, contrast-enhanced micro-CT was previously able to detect damage accumulation between specimens loaded to two levels of secant modulus degradation in machined cortical bone specimens (Landrigan et al., 2011).

Another possible reason for the lack of an increase in SV/TV between loaded groups lies in the use of cyclic three-point bending. Three-point bending subjects only a small volume of tissue near the midspan and periosteal surfaces to the maximum stress, which may have resulted in damage accumulation within a small localized region of tissue that appeared as the same SV in micro-CT. Other limitations associated with cyclic bending tests are well-known (Landrigan and Roeder, 2009); however, the complex morphology of whole rat femora necessitated a simple, reproducible test setup which was afforded by three-point bending. During preliminary testing, the original upper load support – a 4 mm diameter cylinder, identical to the lower supports – was observed to indent the specimen surface; therefore, a new upper load support was designed to more closely approximate the curvature of the diaphysis and minimize contact stresses (Fig. 1). The modified upper load support alleviated the problem of indention, but was unable to perfectly match the variable curvature of every femur leading to variable contact, which may have changed with an increased number of loading cycles. Note that the lower supports did not cause indention and were located outside the region of interest imaged by micro-CT. Finally, the use of a three-point bending support span of sufficient length was prevented by the length of rat femora (Turner and Burr, 1993) and resulted in elevated shear stresses near the midspan. This was the most likely cause for the elevated tensile principal strains and segmented microdamage observed in the medial and lateral anatomic quadrants near the mid-coronal plane, but requires further investigation on the entire cohort of specimens.

5. Conclusions

Fatigue microdamage in whole rat femora loaded in cyclic three-point bending *in vitro* was detected and observed to accumulate at specific spatial locations within the cortex using contrast-enhanced micro-CT. The amount of microdamage measured by micro-CT was significantly greater for groups loaded to a 5% or 10% reduction in secant modulus compared to the control group, but the difference between loaded groups was not statistically significant. At least one distinct region of microdamage, as indicated by the segmented SV, was visible after segmentation in 85% of loaded specimens. A specimen-specific finite element model confirmed elevated tensile principal strains in regions of tissue corresponding to the accumulated microdamage. These regions were not always located where one might expect *a priori* based upon Euler–Bernoulli beam theory, demonstrating the utility of contrast-enhanced micro-CT for non-destructive, 3-D detection of fatigue microdamage in whole bones *in vitro*.

Conflict of interest statement

The authors have no conflicts of interest to disclose.

Acknowledgements

References

Burr, D.B., Forwood, M.R., Fyhrie, D.P., Martin, R.B., Schaffler, M.B., Turner, C.H., 1997. Bone microdamage and skeletal fragility in osteoporotic and stress fractures. Journal of Bone and Mineral Research 12, 6–15.

Burr, D.B., Turner, C.H., Naick, P., Forwood, M.R., Ambrosius, W., Hasan, M.S., Pidaparti, R., 1998. Does microdamage accumulation affect the mechanical properties of bone? Journal of Biomechanics 31, 337–345.

Chapurlat, B.D., Delmas, P.D., 2009. Bone microdamage: a clinical perspective. Osteoporosis International 20, 1299–1308.

Danova, N.A., Colopy, S.A., Radtke, C.L., Kalscheur, V.L., Markel, M.D., Vanderby Jr., R., McCabe, R.P., Escarcega, A.J., Muir, P., 2003. Degradation of bone structural properties by accumulation and coalescence of microcracks. Bone 33, 197–205.

Deuerling, J.M., Rudy, D.J., Niebur, G.L., Roeder, R.K., 2010. Improved accuracy of cortical bone mineralization measured by polychromatic microcomputed tomography using a novel high mineral density composite calibration phantom. Medical Physics 37, 5138–5145.

Forwood, M.R., Parker, A.W., 1989. Microdamage in response to repetitive torsional loading in the rat tibia. Calcified Tissue International 45, 47–53.

Frost, H.M., 1960. Presence of microscopic cracks in vivo in bone. Henry Ford Hospital Medical Bulletin 8, 25–35.

Kotha, S.P., Hsieh, Y.-F., Strigel, R.M., Muller, R., Silva, M.J., 2004. Experimental and finite element analysis of the rat ulnar loading model-correlations between strain and bone formation following fatigue loading. Journal of Biomechanics 37, 541–548.

Landrigan, M.D., Roeder, R.K., 2009. Systematic error in mechanical measures of damage during four-point bending fatigue of cortical bone. Journal of Biomechanics 42, 1212–1217.

Landrigan, M.D., Flatley, J.C., Turnbull, T.L., Kruzic, J.J., Ferracane, J.L., Hilton, T.J., Roeder, R.K., 2010. Detection of dentinal cracks using contrast enhanced micro-computed tomography. Journal of the Mechanical Behavior of Biomedical Materials 3, 223–227.

Landrigan, M.D., Li, J., Turnbull, T.L., Burr, D.B., Niebur, G.L., Roeder, R.K., 2011. Contrast-enhanced micro-computed tomography of fatigue microdamage accumulation in human cortical bone. Bone 48, 443–450.

Lee, T.C., Mohsin, S., Taylor, D., Parkesh, R., Gunnlaugsson, T., O'Brien, F.J., Giehl, M., Gowin, W., 2003. Detecting microdamage in bone. Journal of Anatomy 203, 161–172.

Leng, H., Wang, X., Ross, R.D., Niebur, G.L., Roeder, R.K., 2008. Micro-computed tomography of fatigue microdamage in cortical bone using a barium sulfate

contrast agent. Journal of the Mechanical Behavior of Biomedical Materials 1, 68–75.

Mohsin, S., O'Brien, F.J., Lee, T.C., 2006. Microcracks in compact bone: a three-dimensional view. Journal of Anatomy 209, 119–124.

Moreno, L.D., Waldman, S.D., Grynpas, M.D., 2006. Sex differences in long bone fatigue using a rat model. Journal of Orthopaedic Research 24, 1926–1932.

Norman, T.L., Wang, Z., 1997. Microdamage of human cortical bone: incidence and morphology in long bones. Bone 20, 521–525.

Norman, T.L., Yeni, Y.N., Brown, C.U., Wang, X., 1998. Influence of microdamage on fracture toughness of the human femur and tibia. Bone 23, 303–306.

O'Brien, F.J., Taylor, D., Lee, T.C., 2003. Microcrack accumulation at different intervals during fatigue testing of compact bone. Journal of Biomechanics 36, 973–980.

O'Brien, F.J., Taylor, D., Dickson, G.R., Lee, T.C., 2000. Visualization of three-dimensional microcracks in compact bone. Journal of Anatomy 197, 413–420.

Pattin, C.A., Calert, W.E., Carter, D.R., 1996. Cyclic mechanical property degradation during fatigue loading of cortical bone. Journal of Biomechanics 29, 69–79.

Schaffler, M.B., Radin, E.L., Burr, D.B., 1989. Mechanical and morphological effects of strain rate on fatigue of compact bone. Bone 10, 207–214.

Schaffler, M.B., Choi, K., Milgrom, C., 1995. Aging and matrix microdamage accumulation in human compact bone. Bone 17, 521–525.

Schaffler, M.B., Pitchford, W.C., Choi, K., Riddle, J.M., 1994. Examination of compact bone microdamage using back-scattered electron microscopy. Bone 15, 483–488.

Silva, M.J., Uthgenannt, B.A., Rutlin, J.R., Wohl, G.R., Lewis, J.S., Welch, M.J., 2006. In vivo skeletal imaging of 18F-fluoride with positron emission tomography reveals damage- and time-dependent responses to fatigue loading in the rat ulna. Bone 39, 229–236.

Turner, C.H., Burr, D.B., 1993. Basic biomechanical measurements of bone: a tutorial. Bone 14, 595–608.

Uthgenannt, B.A., Silva, M.J., 2007. Use of the rat forelimb compression model to create discrete levels of bone damage in vivo. Journal of Biomechanics 40, 317–324.

Van Lenthe, G.H., Voide, R., Boyd, S.K., Müller, R., 2008. Tissue modulus calculated from beam theory is biased by bone size and geometry: implications for the use of three-point bending tests to determine bone tissue modulus. Journal of Biomechanics 43, 717–723.

Wang, X., Masse, D.B., Leng, H., Hess, K.P., Ross, R.D., Roeder, R.K., Niebur, G.L., 2007. Detection of trabecular bone microdamage by micro-computed tomography. Journal of Biomechanics 40, 3397–3403.